Towards photoassociation processes of ultracold rubidium trimers

Jan Schnabel [1,*] Tobias Kampschulte,[2] Simon Rupp [2] Johannes Hecker Denschlag [2] and Andreas Köhn [1,†]

[1]*Institute for Theoretical Chemistry and Center for Integrated Quantum Science and Technology, University of Stuttgart, 70569 Stuttgart, Germany*

[2]*Institut für Quantenmaterie and Center for Integrated Quantum Science and Technology, Universität Ulm, 89069 Ulm, Germany*

We theoretically investigate the prospects for photoassociation (PA) of Rb_3, in particular at close range. We provide an overview of accessible states and possible transitions. The major focus is placed on the calculation of equilibrium structures, the survey of spin-orbit effects, and the investigation of transition dipole moments. Furthermore we discuss Franck-Condon overlaps and special aspects of trimers including the (pseudo) Jahn-Teller effect and the resulting topology of adiabatic potential-energy surfaces. With this we identify concrete and suitable PA transitions to potentially produce long-lived trimer bound states. Calculations are performed using the multireference configuration-interaction method together with a large-core effective core potential and a core-polarization potential with a large uncontracted even-tempered basis set.

I. INTRODUCTION

Ultracold molecules offer great opportunities for research and applications, as they can be prepared in precisely defined quantum states [1–6]. Besides studying the molecular properties with high precision, collisions and chemical reactions can then be investigated in the quantum regime where only a single partial wave contributes. Furthermore, cold molecules have a number of applications, ranging from metrology to quantum sensors, to quantum simulation and computation [2,5]. In recent years a number of ways to produce cold molecules have been developed ranging from buffer gas cooling, slowing and filtering, laser cooling, to associating ultracold atoms. The coolest temperatures and the highest control in preparing the molecular quantum state have been typically achieved by associating ultracold atoms [1,3,4]. In this way a variety of different ultracold diatomic molecules has been produced, typically consisting of alkali-metal atoms, such as Li_2, Na_2, K_2, Rb_2, Cs_2, NaRb, RbCs, RbK, NaK, LiNa, LiK, LiRb, LiCs, and NaCs, but there are also other compounds, such as LiYb and RbYb; see, e.g., Refs. [2–4,6] and references therein. Possible methods for the molecule production are, e.g., three-body recombination [7–9], photoassociation (PA) [10,11], and sweeping over a Feshbach resonance [12,13].

Alkali-metal dimer systems have also been studied theoretically in great detail. Accurate potential-energy curves (PECs), dipole moments, and spin-orbit interactions can be obtained via several *ab initio* methods [14]. Among others, the Fourier grid Hamiltonian method [15,16] or the discrete variable representation method [17] were used to analyze the level structure of the well-known coupled $A\,^1\Sigma_u^+ - b\,^3\Pi_u$ manifold in homonuclear alkali-metal dimers.

Producing and understanding ultracold alkali-metal trimers (e.g., X_2Y, X_3, etc., with $X, Y \in \{Li, Na, K, Rb, Cs\}$) clearly is a next milestone. Alkali-metal trimers are much more complex and challenging as compared to alkali-metal dimers, both from the theoretical and the experimental point of view. One aspect of the complexity of an alkali-metal trimer is that many of its levels are prone to quick decay due to fast internal relaxation and dissociation mechanisms. This makes it challenging to prepare and manipulate the trimer on the quantum level. Indeed, detailed and highly resolved spectroscopy on free trimer molecules is generally still lacking. Ultracold trimers have not been produced yet, apart from the extremely weakly bound Efimov states [9,18], which are fast-decaying three-body states of resonantly interacting atoms. Alkali-metal trimers at mK temperatures, however, have been produced in experiments using supersonic beam expansion of Ar seeded with, e.g., sodium atoms, as in Refs. [19–21], or in experiments with alkali-metal clusters formed on helium droplets [22–26]. Theoretical interest in alkali-metal clusters goes back to the 1980s and 1990s, with a number of pioneering works [27–33] giving insights into the electronic properties of alkali-metal trimers, the corresponding ground-state potential-energy surfaces (PESs) and the occurring Jahn-Teller (JT) effect. Yet, these studies were restricted to light alkali-metal species, i.e., Li, Na, and K. Later, following the success of the helium droplet method, theoretical investigations of alkali-metal trimer systems were reappearing—now also containing heavier elements such as Rb [34–40]. In these works, the main focus was on selected JT states and the reproduction of special transitions and spectra measured with He droplet spectroscopy. In recent years, the advent of experiments studying ultracold collisions between an alkali-metal atom and an alkali-metal dimer also triggered further calculations of ground-state alkali-metal trimer PESs. For an overview see, e.g., Ref. [1].

A promising approach for preparing isolated trimer molecules in precisely defined quantum states is PA which

*schnabel@theochem.uni-stuttgart.de
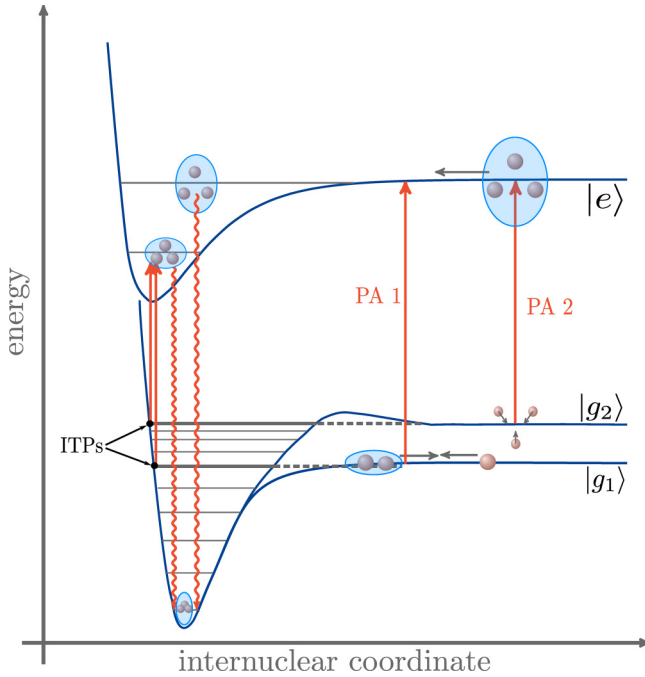
†koehn@theochem.uni-stuttgart.de

FIG. 1. Strongly simplified illustration of the two different photoassociation (PA) schemes for the production of Rb_3 species. PA 1 photoassociates a Rb_2 dimer with a free Rb atom starting from the asymptote $|g_1\rangle$. PA 2 photoassociates three Rb atoms starting from the asymptote $|g_2\rangle$. Both PA processes can be also realized (in principle) starting from an inner turning point (ITP), as discussed in Sec. III A and indicated on the very left. In both cases the excited trimer (more weakly bound for PA starting from $|g_1\rangle$ or $|g_2\rangle$) can radiatively decay to the ground state.

so far has been used for creating dimers in the ultracold regime [10,11]. In a PA process a colliding atom pair in the electronic ground state and a laser photon are transferred into a well-defined bound, electronically excited state $|e\rangle$ [11]. From there, the excited molecule can spontaneously decay into a number of rovibrational, long-lived levels of the molecular ground-state manifold $|g\rangle$. In analogy, one can in principle think of two possible PA schemes for the production of trimer molecules (see Fig. 1).

(i) A dimer molecule and a free ground-state atom are photoassociated ($\equiv$ PA 1). This is shown in Fig. 1. The laser photon drives a transition from the asymptote $|g_1\rangle$ to an electronically excited bound state $|e\rangle$ of the trimer complex. From there it can spontaneously relax to the ground state.

(ii) Three colliding free atoms are photoassociated ($\equiv$ PA 2). As shown in Fig. 1, the photon drives the transition now from the asymptote $|g_2\rangle$ to the excited trimer state.

The PA can in principle take place at long range (large internuclear distances) or at short range (small internuclear distances). Photoassociation at large distances was recently discussed theoretically in Ref. [41]. Here, we therefore rather focus on trimer photoassociation at short distances. Recent theoretical work in Ref. [42], however, suggests that the simultaneous collision of three atoms is strongly suppressed due to an effective repulsive barrier in the short range of the three-body potential, rendering the realization of PA2 at short range less likely. For PA1, however, such a restriction

is not expected. Working out concrete schemes for trimer PA requires detailed knowledge of the involved trimer states and the optical transitions between them. With the present paper we provide a broad overview of states in terms of energy levels and the topology of PESs. Previous theoretical studies on alkali-metal trimers [25–39,43] were essentially restricted to either the doublet or quartet ground state or they investigated selected JT distorted excited states. Furthermore, we calculate the electronic dipole transition matrix elements between states. We discuss special aspects of trimers including different coordinate systems, the (pseudo) Jahn-Teller effect, the Renner-Teller (RT) effect for linear configurations, as well as accidental degeneracies. Finally, we suggest specific PA transitions and investigate coupling effects in terms of spin-orbit interaction. Our paper is intended as a basis for further detailed investigations of PA, which at the next stage will require the simulation of nuclear dynamics.

This paper is organized as follows. Section II briefly introduces the computational aspects and convenient coordinate systems for trimers. Hereafter we discuss major topological features of the corresponding PESs by means of special cuts and comment on the (pseudo) Jahn-Teller (and Renner-Teller) effect. Here, we additionally provide an overview of the expected quartet and doublet equilibrium states of the trimer system within a certain energy range and comment on spin-orbit coupling (SOC) effects and estimate their magnitude. In Sec. III we analyze the excited electronic states with regard to their applicability in PA processes. We find that they can be reached conveniently via the inner turning points on the quartet ground-state PES. We identify one component of the $1\,^4E''$ Jahn-Teller pair as a promising candidate for PA experiments. We thoroughly investigate its suitability as a target state by studying electronic transition dipole strengths with the quartet ground state, spin-orbit coupling and further mixing effects with other states in its close proximity, as well as its distance from conical intersections (COINs). Finally, we summarize the main points of this paper in Sec. IV and give an outlook to ongoing work.

II. GENERAL OVERVIEW OF THE RUBIDIUM TRIMER SYSTEM

A. Computational aspects

Since investigating PA processes of Rb_3 requires an extensive survey of a large number of expected states and transitions in the Rb_3 system, a pragmatic but considerably accurate computational approach has to be applied. In this paper, we are using a large-core effective core potential (ECP) in combination with a core-polarization potential (CPP) as it has been developed in Ref. [44] with a large [$15s12p7d5f3g$] (uncontracted and even-tempered) basis set (UET15); see Supplemental Material [45] for details. In doing so merely the valence electron of Rb is treated explicitly while the remaining 36 electrons are described by the ECP. The CPP accounts for dynamic polarization of the core electrons by the valence electrons. All doublet and quartet states of Rb_3 within a certain energy range were computed using the internally contracted multireference configuration-interaction (MRCI) method [52–56]. As we are only dealing with an effective

TABLE I. Comparison of experimental (references given in square brackets) and calculated values for some spectroscopic constants of a few Rb_2 states. D_e is the dissociation energy, R_e the equilibrium distance, and T_e the electronic term energy. Calculations are performed at MRCI(ECP+CPP)/$15s12p7d5f3g$ level of theory. We also report differences Δ between theory and experiment as well as the mean difference $\bar{\Delta}$ and the absolute mean difference $\bar{\Delta}_{abs}$ for the given set of states.

State	D_e [cm^{-1}]			R_e [Å]			T_e [cm^{-1}]		
	This work	Expt.	Δ	This work	Expt.	Δ	This work	Expt.	Δ
$X\,^1\Sigma_g$ [58]	4116	3993.593	122	4.1689	4.2099	-0.0410	0	0	0
$a\,^3\Sigma_u$ [58]	250	241.503	8	6.0065	6.0940	-0.0875	3866		
$b\,^3\Pi_u$ [59]	7218	7039	179	4.1537	4.1329	0.0208	9632	9601	31
$A\,^1\Sigma_u$ [59]	6071	5981	90	4.8637	4.8737	-0.0100	10778	10750	28
$(2)\,^1\Sigma_g$ [60,61]	3140	2963	177	5.4081	5.4399	-0.0318	13709	13602	107
$(1)\,^1\Pi_u$ [62]	2150	1907	243	4.5203			14700	14666	34
$(1)\,^1\Pi_g$ [63]	1246	1290	-44	5.4225	5.4188	0.0037	15604	15510	94
		$\bar{\Delta}$:	111			-0.0243			59
		$\bar{\Delta}_{abs}$:	123			0.0325			59

three-electron system, the MRCI method has no problem with the separability of the wave function. This means that the PESs are entirely well defined and show correct dissociation behavior into three noninteracting Rb atoms. All calculations are performed using the MOLPRO 2018.2 program package [57].

The pragmatic ECP+CPP approximation is sufficient for gaining a reliable understanding of the physics of the system, as shown in the following, while saving tremendously on computational costs. By construction, the ECP reproduces the experimentally determined atomic energy levels up to the ^2F state [44]. The results in Table I illustrate the expected accuracy for molecular systems—here in terms of benchmark calculations for spectroscopic constants of selected singlet and triplet states of Rb_2 in comparison to experimental results. The calculations do not account for spin-orbit coupling effects, which are only rather small perturbations in most cases. This we will also show in the present paper for Rb_3. The mean differences $\bar{\Delta}$ reported in Table I show a systematic overestimation of the binding energies by 100 to 250 cm^{-1}, while equilibrium distances are typically underestimated by 0.01 to 0.04 Å. This over- and underestimation is a well-known bias introduced by the large-core ECPs due to the approximate description of the repulsion of the core electrons [64,65]. For the electronic term energies T_e, the errors are on the order of 30 to 100 cm^{-1}. Since the Rb_3 system forms three Rb-Rb bonds, we can estimate the accuracy of our *ab initio* method from the above mean errors by $\approx \pm 300$ cm^{-1}. For bond lengths the same accuracy as for Rb_2 is expected (about 1% of the total predicted distance). According to the above experience, binding energies are probably mostly overestimated while bond lengths are underestimated. While these deviations seem large from a spectroscopist's point of view, we note that these deviations are already within the regime of accurate quantum chemical methods, typically defined by the "chemical accuracy" level of $\approx \pm 1$ kcal/mol $\approx \pm 350$ cm^{-1} for energies. Increasing this accuracy is possible but requires steeply increasing computational resources, while our present approach only requires approximately 40 min on eight cores for solving for 27 electronic states at a given Rb_3 geometry, thus allowing one to explore the configurational space efficiently.

B. Coordinates

The atoms of nonlinear triatomic molecular systems always define a plane, which we choose, without loss of generality, as the xz plane; see Fig. 2(a). The system has three internal degrees of freedom, with the only exception of linear geometries for which the system has a fourth degree of freedom. There are many coordinate systems available for properly studying the physics of the system—like the well-known Jacobi and hyperspherical coordinates; see, e.g., Ref. [66] and references therein. In general every coordinate system has its strengths and weaknesses and the choice strongly depends on what one wants to analyze. In this paper we are making use of three different coordinate systems which are introduced in the following.

It is straightforward to use *internuclear distances* as shown in Fig. 2(a). However, not every triple of numbers (R_{12}, R_{23}, R_{13}) obeys the triangular condition and defines a possible molecular configuration. It is convenient to employ *perimetric coordinates* [67–73], as used by Davidson in his analysis of H_3 [74]. Given the set of internal coordinates $\{R_{12}, R_{23}, R_{13}\}$, the perimetric coordinates can be expressed as

$$R_1 = \tfrac{1}{2}(R_{12} + R_{13} - R_{23}), \tag{1a}$$

$$R_2 = \tfrac{1}{2}(R_{12} + R_{23} - R_{13}), \tag{1b}$$

$$R_3 = \tfrac{1}{2}(R_{13} + R_{23} - R_{12}). \tag{1c}$$

The perimetric coordinates are the radii of mutually tangent circles centered on each nucleus [as shown in Fig. 2(b)]. The general topology of this coordinate system reveals some properties.

(a) Every triple of numbers (R_1, R_2, R_3) in the positive octant [see Fig. 2(c)] gives a unique molecular conformation (modulo permutational inversion); i.e., the coordinates satisfy the triangular inequality.

(b) Internuclear distances are given as the sum of the corresponding perimetric coordinates (e.g., $R_{12} = R_1 + R_2$).

(c) Linear molecules are found at the three equivalent boundary planes of the positive octant, where one of the perimetric coordinates is zero (e.g., for $R_1 = 0$, $R_2 = R_{12}$, and $R_3 = R_{13}$).
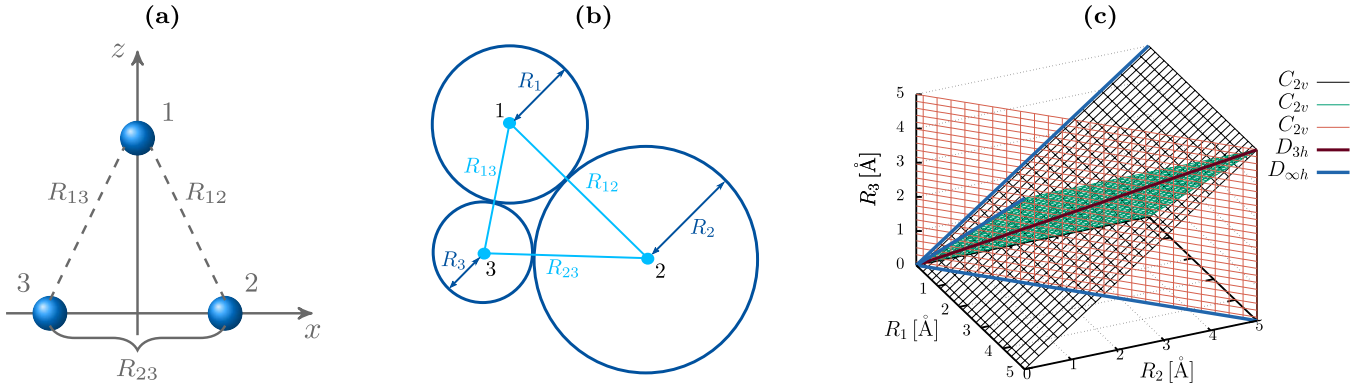
FIG. 2. (a) Sketch of the Rb_3 system in the *xz* plane with *internuclear distances* R_{12}, R_{23}, R_{13}. (b) Illustration of the geometric interpretation of the *perimetric coordinates* for triatomic molecules. They represent the radii of three mutual tangent circles centered on the nuclei. (c) Division of the positive octant in perimetric coordinates to show special configuration subspaces of triatomic systems (i.e., $D_{\infty h}$, D_{3h}, and C_{2v}).

(d) The dissociation limits (atom + dimer) are obtained by one of the coordinates being large (e.g., $atom_1 + dimer_{23} \Leftrightarrow R_1 \to \infty$).

The positive octant contains further special positions (i.e., configurations higher than C_s symmetry) summarized in Fig. 2(c). Linear molecules of $D_{\infty h}$ symmetry are found on three equivalent diagonals of the boundary planes. Equilateral triangular configurations (D_{3h} symmetry) correspond to the space diagonal while isosceles triangles (i.e., C_{2v} symmetry) are, due to the permutational symmetry, represented via one of the three equivalent space diagonal surfaces [note that strictly speaking there are six equivalent subspaces of C_{2v} configurations since it is not defined if the atoms are labeled clockwise or counterclockwise—transition to the inverted structure takes place over a linear one ($R_i = 0$)]. In the context of this paper the perimetric coordinates are a powerful tool for investigating the configuration space (see Sec. III A) of equilibrium states of Rb_3 helping to identify appropriate states for PA processes.

Since homonuclear (alkali-metal) triatomics are prominent systems showing the JT effect [34–37,75,76] it is also useful to introduce the *(symmetry-adapted) JT coordinates* to characterize the corresponding major topological features [COIN seam, Mexican-hat-like PES, and triply degenerate COINs for pseudo Jahn-Teller (PJT) interactions] near D_{3h} equilateral triangular conformations. Given the internuclear distances (R_{12}, R_{23}, R_{13}) they are defined by [76]

$$
\begin{pmatrix} Q_1 \\ Q_2 \\ Q_3 \end{pmatrix} = \begin{pmatrix} \sqrt{1/3} & \sqrt{1/3} & \sqrt{1/3} \\ -\sqrt{1/2} & \sqrt{1/2} & 0 \\ -\sqrt{1/6} & -\sqrt{1/6} & \sqrt{2/3} \end{pmatrix} \cdot \begin{pmatrix} R_{12} \\ R_{13} \\ R_{23} \end{pmatrix}.
$$

(2)

They describe the planar vibrational modes of the system where Q_1 is associated with the breathing mode (preserving D_{3h} geometry), Q_2 with the asymmetric stretch mode (distorting the equilateral triangle into a C_s configuration), and Q_3 with the symmetric stretch mode (taking the system into a C_{2v} conformation). Note that this only holds for D_{3h} symmetry; in the subspace of lower symmetry, e.g., C_{2v}, the actual modes are mixtures of Q_1 and Q_3. Using this set of coordinates, e.g., Hauser *et al.* studied several aspects of the JT effect in K_3 and Rb_3 [34–36] by C_{2v} cuts [one- and two-dimensional (2D)] through the PESs of both species. We are applying these coordinates for investigating the $1\,^4E''$ state in the context of PA experiments in Sec. III C.

C. Special cuts through the PESs

To get an idea of the system's physics, in particular the occurring coupling and crossing effects, we start with analyzing special cuts through the PESs of both doublet and quartet manifolds. For this we restrict our investigations to the C_{2v} subspace since it turns out that all equilibrium structures show at least C_{2v} symmetry. Therefore we are labeling the resulting electronic states according to the irreducible representations (IRREPs) of this point group. Given the choice of coordinates shown in Fig. 2(a), A_1 and B_1 states are symmetric, and A_2 and B_2 states are antisymmetric with respect to reflection of the electronic coordinates at the molecular plane. Figure 3 gives a first impression of the topology of the potential-energy landscapes for the quartet ground state ($1\,^4B_1$) and the first excited quartet state ($1\,^4A_2$) in terms of two-dimensional cuts for C_{2v}-symmetric nuclear configurations. These correspond to one of the space diagonal surfaces shown in Fig. 2(c). The quartet ground state ($1\,^4B_1$) in Fig. 3(a) is well isolated from excited quartet states (i.e., crossings with other states only appear at energies high above the minimum and the dissociation limit of this state) with the global minimum occurring at equilateral triangular (D_{3h}) geometry [40]. At a symmetric linear geometry (for this cut at $R_1 = 0$) we obtain a saddle point marking the transition to the inverted structure. Moreover, we note that the PES of the $1\,^4B_1$ state is rather shallow. These properties have also been pointed out by Sol-
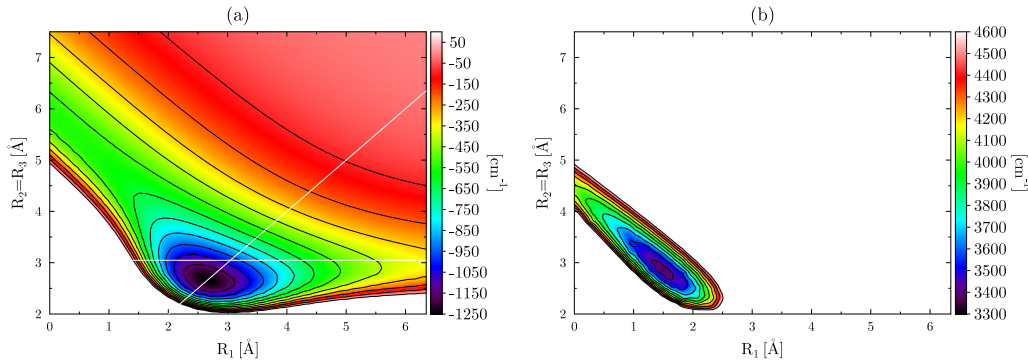
FIG. 3. Two-dimensional contour plots of the quartet ground state $1\,^4B_1$ (a) and the first quartet excited state $1\,^4A_2$ (b) PESs in the subspace R_1 and $R_2 = R_3$ of perimetric coordinates, i.e., along one space diagonal surface in Fig. 2(c). The space diagonal (i.e., D_{3h} configurations) corresponds to the diagonal line shown in white, while the horizontal line [both in (a)] represents the special one-dimensional C_{2v} cut for $R_{23} = 6.094$ Å. The wavy character in (b) is due to the underlying spline interpolation of the corresponding *ab initio* data.

dán in his work concerning the quartet ground state of Rb_3 in Ref. [40]. Figure 3(b) shows the first excited quartet state ($1\,^4A_2$ in C_{2v}) with the global minimum occurring at isosceles triangular (i.e., C_{2v}) geometry. This is due to the JT effect forming a twofold degenerate E'' state (with $1\,^4B_2$) at D_{3h} geometries (this will be discussed in more detail in Sec. III C). This PES rises significantly steeper than the shallow quartet ground-state PES.

The presence of (pseudo) Jahn-Teller interactions can be also observed from one-dimensional scans along the D_{3h} subspace, i.e., along the diagonal shown in white in Fig. 3(a). The resulting PECs are shown in Fig. 4 in the space of internal coordinates ($R_{12} = R_{23} = R_{13}$).

Equilateral triangular configurations of homonuclear triatomics display D_{3h} symmetry and allow for twofold degenerate, so-called E terms (see Table S.VIII in the Supplemental Material [45]). According to the Jahn-Teller theorem [75–80], the PES of at least one of these degenerate states has no extremum at this high-symmetry point. Thus, the system lowers its symmetry to lift the degeneracy, here branching off into $A_1 + B_1$ states for E' or into $B_2 + A_2$ states for E'', respectively. This is accompanied by an energy lowering and the formation of a COIN at the point of degeneracy. This is also indicated by the insets shown in Fig. 4. Potential-energy curves which are degenerate over the whole range shown in Fig. 4 are actually one-dimensional COIN seams in the three-dimensional (3D) configuration space.

The doublet ground states of alkali-metal trimers show their global minimum at obtuse isosceles triangular geometries due to the JT effect (studied theoretically for Li_3 in Refs. [28,29], for Na_3 in Refs. [27–30], for K_3 in Refs. [28,29,34,43], and for Rb_3 in Refs. [36,38,39]). This finding is also illustrated by the corresponding PECs in Fig. 4(a) (and by the alternative one-dimensional cuts in Fig. S3 in the Supplemental Material [45]). A further peculiarity—well known as the PJT effect—is formed, e.g., by the triple of states $\{2\,^2A_1, 2\,^2B_1, 3\,^2A_1\}$, where $2\,^2A_1$ and $2\,^2B_1$ are degenerate components of the $2\,^2E'$ term (for D_{3h} configurations) and the $3\,^2A_1$ state is nearby in energy (near degeneracy)—see Fig. 4(a) and Fig. S3. Consequently, all three states can mix for C_{2v} configurations, which is described within the theory of PJT coupling (see, e.g., Refs. [81,82]).

It follows that due to the third state which is close in energy the COIN seam of the doubly degenerate JT state at high-symmetry geometries vanishes. Only at a *single* point in the D_{3h} subspace all three states become degenerate forming a *triply* degenerate COIN point [30]. This intersection is analogous to the JT one, but it is not required by symmetry (accidental degeneracy). All of this is essential to fully understand the well-known experimentally observed B band in alkali-metal triatomics [75].

In contrast to the doublet ground state, the quartet ground state is free of JT distortions with its global minimum at D_{3h} configuration. The first pair of excited quartet states, however, is degenerate along a one-dimensional COIN seam in the D_{3h} configuration space, and spans a $1\,^4E''$ term, which splits into $1\,^4A_2$ and $1\,^4B_2$ states when the symmetry is lowered. Besides those states which are exactly degenerate, there are also a number of nearly degenerate states. In particular, there are quadruple interactions [39] present within the subset $\mathcal{Q}$ of quartet states:

$$\mathcal{Q} = \{1\,^4A_1, 2\,^4A_1, 2\,^4B_1, 3\,^4B_1\}. \tag{3}$$

This peculiarity can be seen in Fig. 4(b) [and Fig. S3(b) in the Supplemental Material [45]], where those states are almost degenerate in a region reaching from ≈ 5.0 to ≈ 7.0 Å. More details on all JT and PJT pairs within this energy range can be found in the Supplemental Material [45] in Table S.V.

The other one-dimensional cut indicated in Fig. 3(a) corresponds to a collision trajectory between a Rb_2 molecule and a Rb atom. For this cut, we fixed the distance R_{23} to the equilibrium distance of the lowest triplet state ($a\,^3\Sigma_u$) of Rb_2. The resulting cuts in Figs. 4(c) and 4(d) give a first impression of the states possibly involved in a PA 1 scheme. Moreover, this graph shows one dimension of the 2D branching space (formally spanned by Q_2 and Q_3; see Sec. II B) where the degeneracies from high-symmetry configurations (here found at the point $R_{12} = R_{13} = R_{23} = 6.094$ Å) are lifted. This gives a notion of the topology of the full 3D potential-energy landscape. The density of states increases for higher energies for both doublet and quartet manifolds and decreases the chance for finding sufficiently long-lived target states for PA experiments. Therefore and due to the fact that the doublet ground
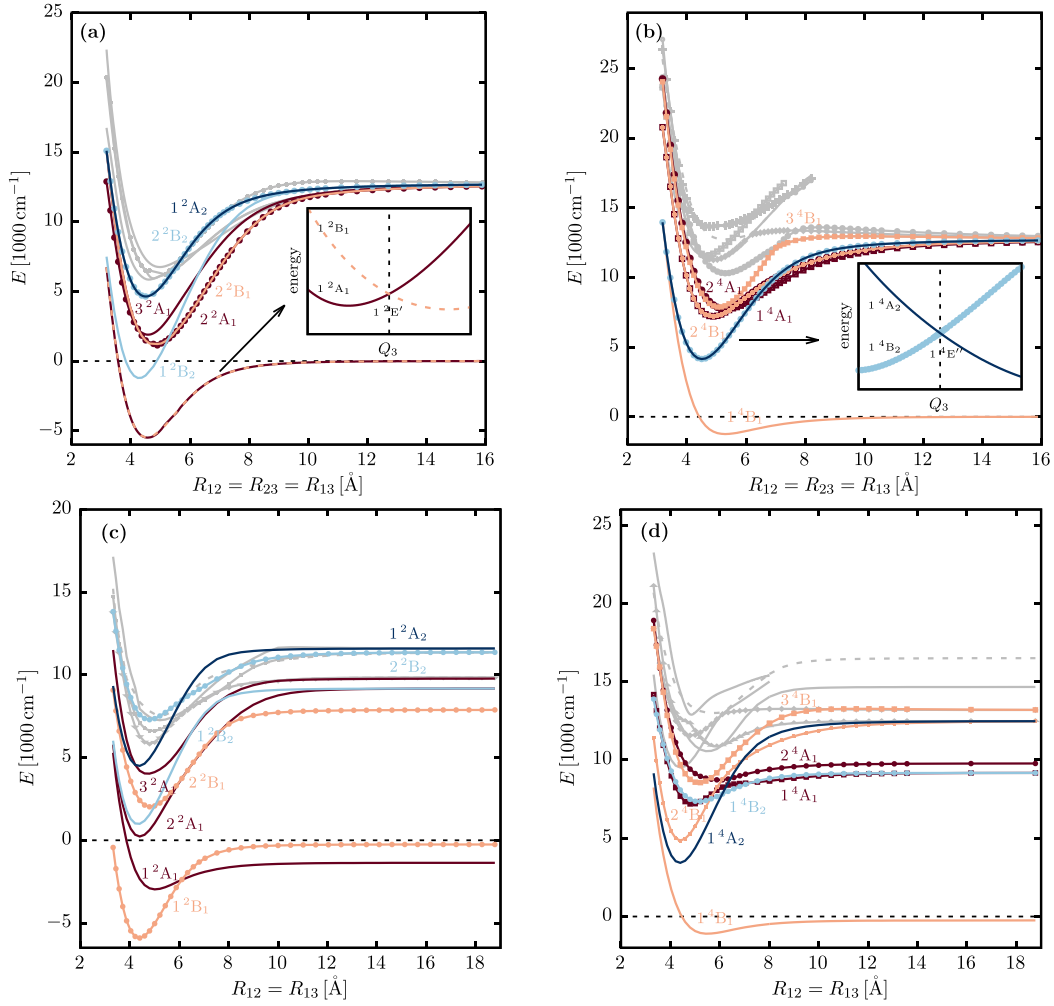
FIG. 4. Upper panel: One-dimensional cut through the potential-energy surfaces (PESs) along the space diagonal in the perimetric coordinate space shown in Fig. 2(c) and in terms of the diagonal shown in Fig. 3(a) (i.e., D_{3h} scan maintaining the equilateral triangular configuration). Doublet states are shown in (a) and quartet states in (b), respectively. The low-lying states discussed in the text are highlighted; the presence of further states is indicated by the gray lines. Lower panel: One-dimensional cut through the PESs along one special direction on one space diagonal surface shown in Fig. 2(c). This C_{2v} scan corresponds to a fixed distance $R_{23} = R_e(a^3\Sigma_u) = 6.094$ Å. Doublets are shown in (c) and quartets in (d), respectively.

state has a rather complex behavior due to JT distortions we focus on quartet states.

Linear configurations of the trimer system are subject to RT or combined PJT plus RT interactions. A detailed analysis of this, however, is beyond the scope of the present paper. Nevertheless, a comment can be found in the Supplemental Material [45].

D. Equilibrium states

A systematic overview of the energy levels of all doublet and quartet states of Rb$_3$ considered in this paper is given in Fig. 5. All energy levels refer to the electronic energy at the equilibrium geometry. For finding the equilibrium states we started from high-symmetry configurations (D_{3h}) and proceeded to geometries of lower symmetry (C_{2v}). Our analysis did not show any evidence for equilibrium structures of even lower symmetry, i.e., C_s. We determined all equilibrium states and their electronic term energies in the energy region up to

the $5s + 2 \times 5p$ asymptote. The energies of the Rb$_2$+Rb or Rb+Rb+Rb dissociation asymptotes are given in the middle panel. The assignment of the trimer states to the Rb$_2$+Rb asymptotes is in general only unique for the quartet ground state $1\,^4B_1$ dissociating into $a^3\Sigma_u + 5s$. For one-dimensional C_{2v} cuts as shown in Figs. 4(c) and 4(d) we obtain a unique assignment for all quartet states and some doublet states as well. However, in the general case, for both doublet and quartet states, all Rb$_2$+Rb asymptotes correlating with the respective trimer state symmetry are possible dissociation channels. Most of the excited states correlate to the $2 \times 5s + 5p$ asymptote. Merely the highly excited quartet states $2\,^4B_2$, $3\,^4B_2$, and $4\,^4A_1$ correspond to the $5s + 2 \times 5p$ asymptote and thus to the $(1)\,^3\Pi_u + 5p$ dissociation limit. The lowest doublet JT manifold $1\,^2E' = 1\,^2A_1 + 1\,^2B_1$ dissociates either to $X\,^1\Sigma_g + 5s$ or to $a^3\Sigma_u + 5s$. The remaining doublet states correspond to Rb$_2$+Rb asymptotes below the $2 \times 5s + 5p$ asymptote where both singlet and triplet Rb$_2$ states are possible. Finally, the top panel of Fig. 5 also shows the ionized states of Rb$_3^+$ appearing
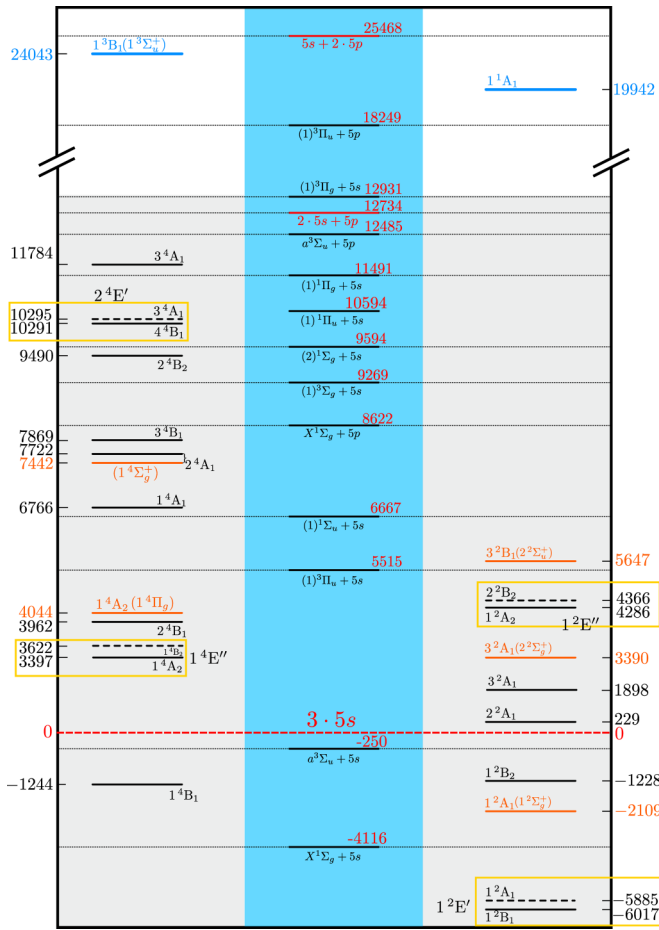
FIG. 5. Energy-level diagram of the extremal points of doublet (right) and quartet (left) states of Rb_3 optimized at MRCI(ECP+CPP)/UET15 level of theory. The dissociation asymptotes into Rb_2+Rb (with the corresponding equilibrium energies of the Rb_2 states) or Rb+Rb+Rb are shown in the area highlighted in blue. Levels given in black belong to triangular equilibrium configurations (i.e., D_{3h} or C_{2v} symmetry) while levels given in orange represent linear equilibrium configurations (all of them $D_{\infty h}$ symmetry). Yellow boxes mark Jahn-Teller states, where the respective dashed lines correspond to saddle points showing isosceles triangular geometry. The ionized Rb_3^+ states are shown at the top in terms of blue energy levels. All energies are given relative to the free atom-atom-atom limit (i.e., $3 \times Rb[5s]$).

in either singlet or triplet configuration. This could be useful if a resonance-enhanced multiphoton ionization [83] scheme is used for the detection of previously generated Rb_3 species. All these results are listed in Table II (for triangular geometries) and in Table III (for linear configurations) together with their corresponding harmonic vibrational frequencies $\tilde{\nu}$.

Our results are in good agreement with previous theoretical studies of Rb_3. For the quartet ground state Soldán [40] found equilateral bond distances b with $b = 5.450$ Å, using the RHF-RCCSD(T) approach with a [16s13p8d5f3g] basis and the small-core ECP from Ref. [84] (ECP28MDF). The energy of the minimum was determined at $E_{\min} = -1071\,\mathrm{cm}^{-1}$. Hauser *et al.* [25,35] found for the equilateral bond distances $b = 5.500$ Å with corresponding energy $E_{\min} = -939\,\mathrm{cm}^{-1}$ and harmonic frequencies

$\{\tilde{\nu}_{D_{3h}}, \tilde{\nu}_{C_{2v}}, \tilde{\nu}_{C_s}\} = \{18, 21, 21\}\,\mathrm{cm}^{-1}$ using RHF-RCCSD(T) with the ECP28MDF small-core ECP and the corresponding original basis set augmented by a $(1s, 1p, 1d)$ set of diffuse functions. In comparison, our computations give a binding energy of $-1244\,\mathrm{cm}^{-1}$, equilateral bond distances of 5.311 Å, and vibrational frequencies of $\{\tilde{\nu}_{D_{3h}}, \tilde{\nu}_{C_{2v}}, \tilde{\nu}_{C_s}\} = \{23.8, 23.6, 23.6\}\,\mathrm{cm}^{-1}$. In case of the doublet ground state Hauser *et al.* [35,36] obtained bond distances with $R_{12} = R_{13} = 4.387$ Å, $R_{23} = 5.575$ Å, and the equilibrium energy $E_{\min} = -5321\,\mathrm{cm}^{-1}$ using RHF-UCCSD(T), small-core ECP, and a [14s, 11p, 6d, 3f, 1g] uncontracted even-tempered basis set derived from the ECP28MDF basis. Our calculations result in bond distances with $R_{12} = R_{13} = 4.379$ Å and $R_{23} = 5.393$ Å with a corresponding binding energy of $-6017\,\mathrm{cm}^{-1}$. Moreover, we can extract the vertical transition energy from the quartet ground state to the high-spin $2\,^4E'$ manifold from Fig. 5 and Table II and compare the result with the one calculated by Hauser *et al.* [25,35] using a modified version of CASPT2 (referred to as RS2C in MOLPRO), the same small-core ECP, as well as the same basis set as described before. Our result is $E_{2\,^4E' \leftarrow 1\,^4A_2'} = 11\,535\,\mathrm{cm}^{-1}$ compared to the result $11\,530\,\mathrm{cm}^{-1}$ of Hauser *et al.* The corresponding experimental value [22,26] is $11\,510\,\mathrm{cm}^{-1}$ referring to the lowest-energy maximum band of the measured band spectra applying laser-induced fluorescence spectroscopy to Rb_3 clusters formed on helium nanodroplets.

In the Supplemental Material [45] in Tables S.III and S.IV and Fig. S2 we provide a more detailed overview on all states, i.e., by including saddle points, obtained within the energy range up to the $5s + 2 \times 5p$ asymptote. Some of the saddle points define the barrier heights between minima on PESs. This becomes important for analyzing the JT effect.

E. Survey of spin-orbit coupling effects

SOC is still a comparatively weak effect for Rb (the SOC induced splitting of the atomic ^2P state is $\approx 240\,\mathrm{cm}^{-1}$) and the classification of states in terms of their total spin, as in the previous sections, is justified. Nevertheless, in particular in the vicinity of degeneracies, SOC can lead to a mixing of states of the same or of different spin. To get an idea of the importance of this phenomenon we have investigated the size of the couplings for selected nuclear configurations at the MRCI(ECP+CPP)/UET15 level of theory using the ECP-LS technique for the corresponding large-core pseudopotential. All important details about the computation of the corresponding spin-orbit matrix based on a pseudopotential approach can be found, e.g., in Refs. [44,85]. The computations included 15 quartet (4/5/3/3) and 12 doublet (5/4/2/1) states, according to the MOLPRO specific ordering of the IRREPs $(A_1/B_1/B_2/A_2)$. That is, in total a 84×84 SO matrix is set up and diagonalized.

To get a qualitative overview we show in Fig. 6 the absolute values of the SO matrix $|\hat{H}_{ij}^{SO}|$ at the equilibrium geometry of the first excited quartet state $1\,^4A_2$ as a heat-map representation. It should look similar for comparable geometrical configurations. The main contributions come from doublet-doublet ($D \leftrightarrow D$), respectively, quartet-quartet ($Q \leftrightarrow Q$) couplings. However, there are also nonvanishing

TABLE II. Synopsis of triangular (C_{2v} and D_{3h}) doublet and quartet (ground and excited) states of Rb$_3$ as well as the singlet state of Rb$_3^+$ computed at MRCI(ECP+CPP)/UET15 level of theory. Equilibrium structures are given in terms of the internal coordinates (perimetric coordinates) introduced in Fig. 2 and all corresponding energies (E_{rel}) are given relative to the ($3 \times 5s$) asymptote calculated at the same level of theory. The states are labeled according to the C_{2v} IRREPs while the corresponding assignment to D_{3h} symmetry is given in parentheses. This complements the results of the energy-level diagram of Fig. 5.

State (D_{3h})	R_{12}, R_{23}, R_{13} [Å] (R_1, R_2, R_3)	Geometry	E_{rel} [cm^{-1}]	$\tilde{\nu}_{D_{3h}}$ [cm^{-1}][a]	$\tilde{\nu}_{C_{2v}}$ [cm^{-1}][a]	$\tilde{\nu}_{C_s}$ [cm^{-1}][a]
$1\,^4B_1$ ($1\,^4A_2'$)	5.311, 5.311, 5.311 (2.656,2.656,2.656)	D_{3h}	-1244	23.8	23.6	23.6
$1\,^4A_2$ ($1\,^4E''$)	4.368,5.700,4.368 (1.518,2.850,2.850)	C_{2v}	3397	50.2	17.2	35.8
$2\,^4B_1$ ($1\,^4E'$)	4.442, 8.179, 4.442 (0.352,4.090,4.090)	C_{2v}	3962	40.3	9.6	40.4
$1\,^4A_1$ ($1\,^4E'$)	4.993, 8.076, 4.993 (0.955,4.038,4.038)	C_{2v}	6766	32.8	9.8	50.7
$2\,^4A_1$ ($1\,^4A_1'$)	5.325, 5.325, 5.325 (2.663,2.663,2.663)	D_{3h}	7722	32.0	83.9	83.9
$3\,^4B_1$ ($2\,^4A_2'$)	5.084, 5.084, 5.084 (2.542,2.542,2.542)	D_{3h}	7869	43.0	58.2	58.2
$2\,^4B_2$ ($2\,^4E''$)	4.443, 6.217, 4.443 (1.335,3.109,3.109)	C_{2v}	9490	52.0	42.7	41.3
$4\,^4B_1$ ($2\,^4E'$)	5.283, 5.337, 5.283 (2.615,2.669,2.669)	C_{2v}	10291	31.5	37.7	39.0
$3\,^4A_1$ (upper) ($2\,^4E'$)	4.687, 7.226, 4.687 (1.074,3.613,3.613)	C_{2v}	11784	41.5	28.2	27.5
$1\,^2B_1$ ($1\,^2E'$)	4.379, 5.393, 4.379 (1.682,2.697,2.697)	C_{2v}	-6017	53.1	20.6	33.3
$1\,^2B_2$ ($1\,^2A_2''$)	4.276, 4.285, 4.276 (2.134,2.143,2.143)	C_{2v}	-1228	60.9	43.9	44.1
$2\,^2A_1$ ($2\,^2E'$)	4.398, 6.073, 4.398 (1.361,3.037,3.037)	C_{2v}	229	50.4	26.7	42.1
$3\,^2A_1$ ($1\,^2A_1'$)	4.557, 4.557, 4.557 (2.279,2.279,2.279)	D_{3h}	1898	51.9	100.6	100.6
$1\,^2A_2$ ($1\,^2E''$)	4.337, 5.132, 4.337 (1.771,2.566,2.566)	C_{2v}	4286	52.9	23.7	30.2
$1\,^1A_1$ ($^1A_1'$)	4.610, 4.610, 4.610 (2.305,2.305,2.305)	D_{3h}	19942	53.2	36.6	36.5

[a]In general the assignment is not unique but usually $\tilde{\nu}_{D_{3h}}$ is Q_1-like, $\tilde{\nu}_{C_{2v}}$ is Q_3-like, and $\tilde{\nu}_{C_s}$ is Q_2-like.

couplings between quartet and doublet states (Q $\leftrightarrow$ D and vice versa). The corresponding selection rules (for C_{2v} configurations), deduced from group theory, allow for $\Delta S = 0, \pm 1$ and couplings between all combinations of IRREPs except the same (a detailed derivation is given in the Supplemental Material [45]).

The explicit values for resulting shifts and zero-field splittings (i.e., the lifting of degenerate states in the absence of a magnetic field) are given in Tables S.XIII– S.XVI in the Supplemental Material [45] for the equilibrium states listed in Tables II and III together with the corresponding most dominantly coupling states. Typical coupling strengths amount to 20 to 70 cm^{-1}, as shown in Fig. 6, but the resulting energy shifts and zero-field splittings are much smaller. For instance the quartet ground state splits into the two states $E_{1/2}$ and $E_{3/2}$ of the D_{3h} spin double group [35], but the corresponding zero-field splitting is less than 0.1 cm^{-1} and the energy lowering induced by the SOC is less than 0.2 cm^{-1}. The same

observation holds for the first excited quartet state $1\,^4A_2$ for which these SOC effects are again smaller than 1 cm^{-1}. The reason for these small values lies in the effective quenching of the orbital angular momentum in triangular geometries and in the energy separation to other states. For highly symmetric configurations, in particular for linear geometries and in the presence of spatial degeneracies, the effects become larger, e.g., for the $1\,^4\Pi_g$ state, for which splittings and energy shifts of up to 200 cm^{-1} are computed.

The strength of SOC, in particular between the quartet ground state $1\,^4B_1$ and the first excited quartet state $1\,^4A_2$, decays with respect to distortions from equilateral triangular geometries. Only in the limit of dissociation into both Rb$_2$+Rb and $3 \times$ Rb SOC effects become larger, since Rb$_2$ always has a well-defined C_∞ axis. To summarize, we do not expect significant SOC induced mixing of the states in the vicinity of equilibrium geometries, in particular for the low-lying states $1\,^4B_1$ and $1\,^4A_2$.

TABLE III. Synopsis of linear ($D_{\infty h}$) doublet and quartet (ground and excited) states of Rb_3 as well as the triplet state of Rb_3^+ computed at MRCI(ECP+CPP)/UET15 level of theory. Equilibrium structures are given in terms of the internal coordinates (perimetric coordinates) introduced in Fig. 2 and all corresponding energies (E_{rel}) are given relative to the $(3 \times 5s)$ asymptote calculated at the same level of theory. The states are labeled according to the C_{2v} IRREPs while the corresponding assignment to $D_{\infty h}$ symmetry is given in parentheses. This complements the results of the energy-level diagram of Fig. 5.

State ($D_{\infty h}$)	R_{12}, R_{23}, R_{13} [Å] (R_1, R_2, R_3)	E_{rel} [cm^{-1}]	$\tilde{\nu}_{symm}$ [cm^{-1}]	$\tilde{\nu}_{asymm}$ [cm^{-1}]	$\tilde{\nu}_{bending_1}$ [cm^{-1}]	$\tilde{\nu}_{bending_2}$ [cm^{-1}]
$1\,^4A_2 + 2\,^4B_1{}^a(1\,^4\Pi_g)$	4.435, 8.869, 4.435 (0.000,4.435,4.435)	4044	33.7	41.7	236.8	84.7
$2\,^4A_1(1\,^4\Sigma_g^+)^b$	4.937, 9.874, 4.937 (0.000,4.937,4.937)	7442	398.2	48.9	282.6	282.6
$1\,^2A_1\ (1\,^2\Sigma_g^+)$	4.795, 9.590, 4.795 (0.000,4.795,4.795)	−2109	24.9	60.8	4.1	4.1
$3\,^2A_1(2\,^2\Sigma_g^+)^b$	4.440, 8.880, 4.440 (0.000,4.440,4.440)	3390	405.9	46.9	313.8	350.3
$3\,^2B_1\ (2\,^2\Sigma_u^+)$	4.930, 9.860, 4.930 (0.000,4.930,4.930)	5647	27.7	48.4	169.6	169.6
$1\,^3B_1\ (^3\Sigma_u^+)$	4.875, 9.749, 4.875 (0.000,4.875,4.875)	24043	30.3	49.7	6.3	6.3

[a]Renner-Teller pair with the $^4B_1$ state turning out as saddle point at this linear configuration.

[b]As a consequence of a combined pseudo Jahn-Teller and Renner-Teller interaction two A_1 states, one of them arising from a Π_u state, can mix for greater displacements along $D_{\infty h}$ geometries. This is also the reason for nondegenerate frequencies $\tilde{\nu}_{bending_{1,2}}$.

FIG. 6. Heat-map representation of the absolute values of the spin-orbit matrix $\sqrt{|\hat{H}_{ij}^{SO}|^2}$ (without diagonal elements). The Rb_3 geometry was fixed to the equilibrium configuration of the first excited quartet state $1\,^4A_2$ (see Table II). The partitioning separates doublet-doublet (D↔D), quartet-quartet (Q↔Q), and quartet-doublet (Q↔D) couplings. The dashed blue lines mark the rows where the four components corresponding to the $1\,^4A_2$ state are found in the SO matrix. The SO matrix is sorted according to IRREPs (C_{2v}) in the sequence ($A_1/B_1/B_2/A_2$) where each of them (in zeroth-order basis) are ordered with respect to increasing energy and are accordingly combined with the m_s spin function starting from $m_s = +1/2$ to $-1/2$ for doublets and $m_s = +3/2$ to $-3/2$ for quartets. This is a complete representation with respect to the energetically lowest 12 doublet (5/4/2/1) and 15 quartet states (4/5/3/3) leading to the 84×84 SO matrix.

III. IDENTIFYING APPROPRIATE STATES FOR PHOTOASSOCIATION

A. Configuration space survey

For the realization of the trimer PA processes, nonvanishing Franck-Condon factors are required, i.e., a significant overlap of the nuclear scattering wave function of Rb_2+Rb or $3 \times Rb$ collisions and the molecular trimer vibrational wave function of the excited state. In this paper we are mostly interested in producing deeply bound trimers close to the vibrational ground state for reasons of increased stability, lifetime, and simplicity. In fact, as we will show in the following, it turns out that the equilibrium geometries of a number of excited states are in close proximity to the ITPs of the scattering wave function. Since the scattering wave function typically exhibits a local maximum at the ITP this suggests that favorable Franck-Condon factors might be found for photoassociating excited trimers in their equilibrium geometry. For trimers, the ITPs are actually 2D surfaces in the configuration space. They correspond to those points where the quartet ground-state PES equals to the energy of the scattering state. For the case of Rb_2+Rb this energy is given by the negative binding energy of the $a\,^3\Sigma_u$ state of Rb_2, i.e., $\approx -250 \text{ cm}^{-1}$, and for the case of $3 \times Rb$ the energy is approximately zero. Again, note that PA2 at short distances is expected to be rather unlikely due to the effective repulsive barrier in the short range of the three-body potential; see Ref. [42]. Nevertheless, at large distances PA2 should be possible. The feasibility for PA1 is shown in Ref. [41]. The locations of the ITPs (i.e., ITP$_{250}$ and ITP$_0$) and the positions of the equilibrium geometries are shown in Fig. 7(a). The equilibrium geometries have at least C_{2v} symmetry and are located on a space diagonal surface, as shown in Fig. 2(c) (due to the threefold degeneracy of C_{2v} and $D_{\infty h}$ configurations, resulting from the indistinguishability of
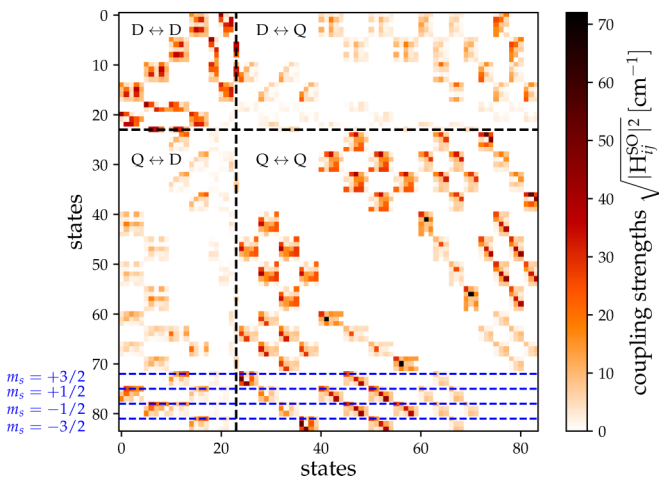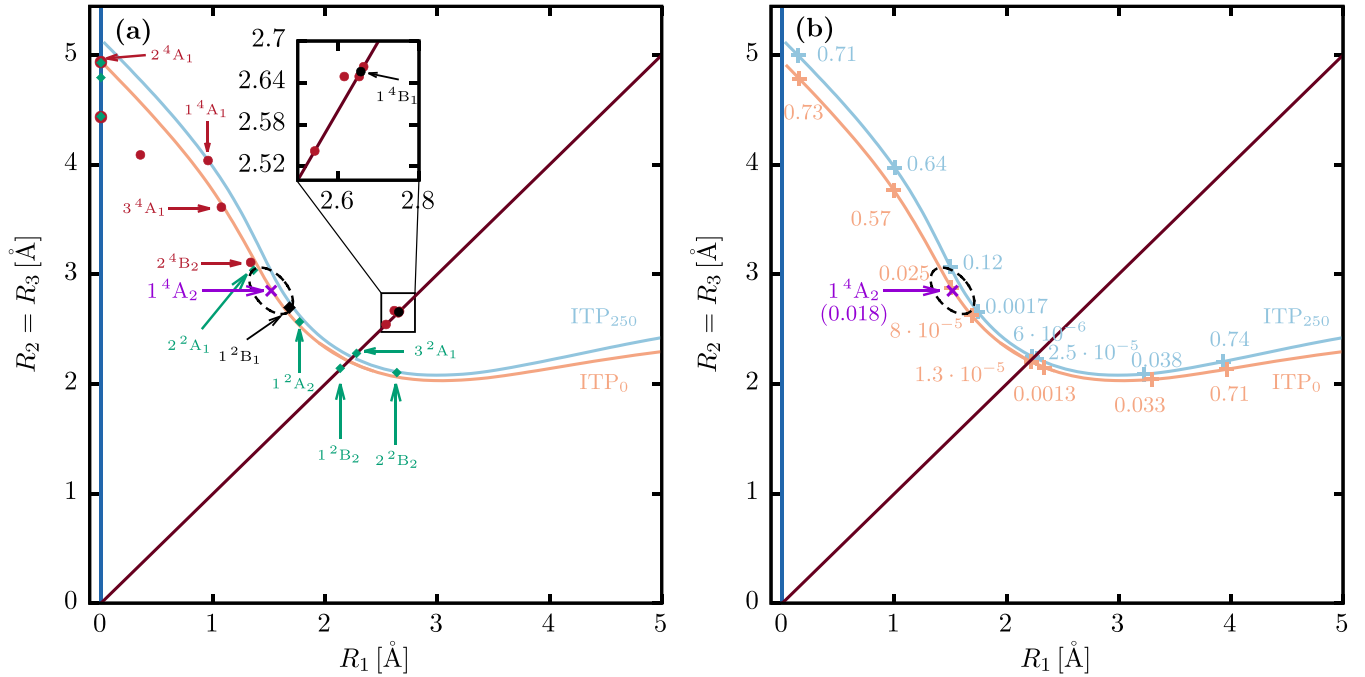
FIG. 7. Inner turning point (ITP) locations and locations of equilibrium geometries in the configuration space of perimetric coordinates. (a) Since all equilibrium geometries show at least C_{2v} symmetry the configuration space survey can be restricted to one of the space diagonal surfaces shown in Fig. 2(c). ITPs on the quartet ground-state PES with respect to either the $Rb_2 + Rb$ or $3 \times Rb$ dissociation scenarios are given in light blue for the first one and in light red for the latter. States lying close to these lines are promising candidates for showing good Franck-Condon factors. Here we focus on the $1\,^4A_2$ state highlighted in purple. The numbers given in (b) along both ITP lines represent the electronic dipole transition strengths (in units of $[D^2]$) between the quartet ground state and this $1\,^4A_2$ state at the corresponding ITP locations. Note that the numbers given in (b) do not correlate with the equilibrium geometries depicted in (a). The transition dipole strength at the equilibrium geometry of the first excited quartet state amounts to $0.018\,D^2$. The ellipses shown in (a) and (b) give an estimate of the size of the vibrational ground-state wave function for the $1\,^4A_2$ state.

the three Rb atoms, there are three equivalent such representations).

B. Electronic dipole transition moments

A successful realization of PA processes also requires nonvanishing electronic dipole transition moments between the initial state and the corresponding excited state. In C_{2v} symmetry electronic dipole transitions between all states (with $\Delta S = 0$) are allowed, except transitions between A_1 and A_2 as well as B_1 and B_2 (a detailed derivation of this as well as for the selection rules in D_{3h} is given in the Supplemental Material [45]). Due to the facts that the density of states increases with increasing energy and that the transition between the quartet ground state and the first excited quartet state ($1\,^4A_2$) is symmetry allowed and in close proximity to the ITP lines, we are going to focus our following investigations on this state.

We study the specific electronic dipole transition strengths (in units of $[D^2]$) at ITP configurations in Fig. 7(b). The magnitudes of the electronic dipole transition strengths between the quartet ground state and the first excited quartet state, $1\,^4A_2$, are approximately the same for ITP_{250} and ITP_0. In both cases we obtained no considerable changes in C_s direction. In the vicinity of D_{3h} configurations (diagonal dark red line) we obtain vanishing transition strengths due to the fact that

for D_{3h} geometries the $1\,^4A_2$ state forms a degenerate $1\,^4E''$ JT state (see Sec. III C for a detailed discussion) where the quartet ground state is described in terms of the A'_2 IRREP. In the Supplemental Material [45] we show that electronic dipole transitions between these states are zero by symmetry. For C_{2v} configurations admixture of other configurations makes the transition dipole moment nonvanishing, but it remains rather small.

Using the harmonic vibrational frequencies in Table II, and the topology of the PES in Fig. 3(b) we can estimate the extent of the vibrational ground-state wave function for the $1\,^4A_2$ state. For each normal mode i the size is approximated by the harmonic oscillator length. It can be derived from the one-dimensional Schrödinger equation of a particle of reduced mass μ (for homonuclear triatomics $\mu = m/\sqrt{3}$) moving in a harmonic potential, yielding (for ^{87}Rb)

$$x_i = \sqrt{\frac{\hbar}{\mu \omega_i}} = \sqrt{\frac{\sqrt{3}\hbar}{100 \times m(^{87}Rb) \times c \tilde{\nu}_i}}. \qquad (4)$$

The PES in this region takes on the form of a rotated ellipse with semimajor axis $a = 0.495\,\text{Å}$ and semiminor axis $b = 0.29\,\text{Å}$ calculated from Eq. (4) using $\tilde{\nu}_{D_{3h}}$ and $\tilde{\nu}_{C_{2v}}$. These findings are indicated in Fig. 7. Since there is a good overlap with the ITPs, a sizable Franck-Condon factor can be expected.
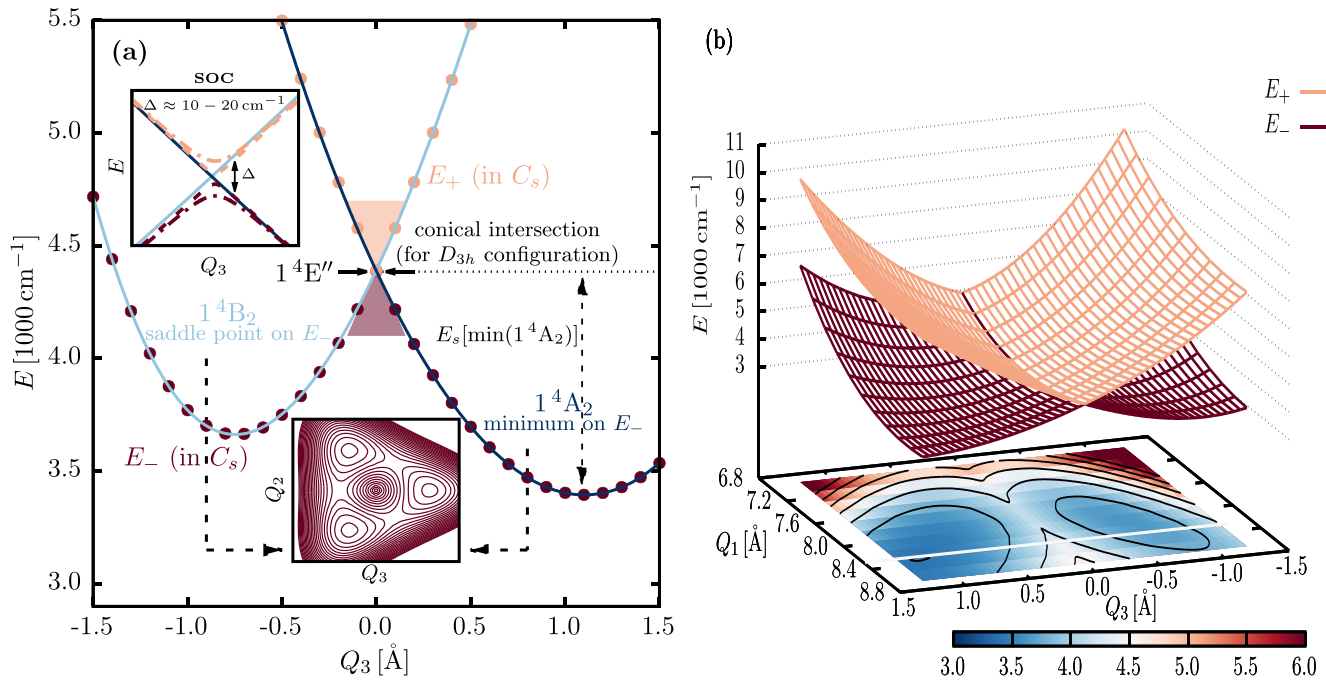
FIG. 8. The quartet states (according to C_{2v} nomenclature) $1\,^4B_2$ and $1\,^4A_2$ forming the Jahn-Teller pair $1\,^4E''$ in the higher-symmetry D_{3h} subspace (equilateral triangle). For each equilateral triangular configuration the two states show a conical intersection (COIN) leading to a COIN seam (one-dimensional curve) in the full 3D configuration space. Lowering the symmetry, e.g., by scanning along the C_{2v} preserving coordinate Q_3, leads to a splitting of both states [see (a) for $Q_1 = 8.335\,\text{Å}$ and $Q_2 = 0.0\,\text{Å}$ fixed]. Due to the Jahn-Teller character these states cannot be viewed separately. The interactions lead to the formation of a lower PES sheet E_- showing tricorn topology (three equivalent wells alternating regularly with three saddle points, separated by the localization energy $E_{\text{loc}} = 225\,\text{cm}^{-1}$) and a parabolic shaped upper surface E_+. The $1\,^4A_2$ state represents a global minimum on E_- while the $1\,^4B_2$ state is a saddle point on this surface. This behavior is illustrated by the lower inset in (a) for $Q_1 = 8.335\,\text{Å}$. Including spin-orbit coupling (SOC) leads to the annihilation of the COIN and to an energy splitting Δ as shown by the inset on the top left in (a). The topology of the PESs in the two-dimensional subspace of Q_1 and Q_3 is shown in (b). The degenerate line at $Q_3 = 0.0\,\text{Å}$, where we have D_{3h} symmetry, corresponds to the one-dimensional COIN seam. The white line at the bottom represents the one-dimensional cut shown in (a).

C. The $1\,^4E''$ Jahn-Teller pair

As indicated in Table II the first excited quartet state $1\,^4A_2$ forms, together with the $1\,^4B_2$ state, for equilateral triangular geometries the JT pair $1\,^4E''$. The two states are degenerate for every high-symmetry (D_{3h}) nuclear configuration, thus forming a one-dimensional COIN seam in the full 3D configuration space as already outlined in Sec. II C. When lowering the symmetry (scanning along Q_2 and/or Q_3) both states branch off forming a lower PES sheet E_- revealing a tricorn topology with three equivalent minima (of $1\,^4A_2$ character) alternating regularly with three saddle points (of $1\,^4B_2$ character) as illustrated by the lower inset in Fig. 8(a). The upper surface E_+ is a paraboloid of revolution about $Q_2 = Q_3 = 0$ [30]. SOC removes the COIN with an energy splitting of $\Delta \approx 10$–$20\,\text{cm}^{-1}$ (i.e., weak SOC) between the corresponding Kramers pairs of E_+ and E_-. For details of the underlying (relativistic) JT theory see, e.g., Refs. [75–80] and Refs. [86–88], respectively, for the effect of SOC on COINs in general. Here it is important to note that due to the JT interaction the $1\,^4A_2$ and $1\,^4B_2$ states cannot be viewed separately. Figure 8(b) illustrates the one-dimensional COIN seam occurring for $Q_2 = Q_3 = 0$ and shows a contour plot of the trough of the E_- PES in the D_{3h}-C_{2v} subspace of Q_1 and Q_3. The energetically lowest COIN occurs at $R_1 = R_2 = R_3 =$

$2.250\,\text{Å}$ with an energy $E_{\text{min(COIN)}} = 4146\,\text{cm}^{-1}$ (note that a detailed overview on all JT pairs is given in Table S.V in the Supplemental Material [45]). It is convenient [30] to define a stabilization energy E_s of the minima on E_- from the COINs as well as a localization energy E_{loc} defining the barrier height in the tricorn potential. In the lower inset of Fig. 8(a) this denotes the energy barrier for transitions between the three equivalent minima on E_- separated by three saddle points. The stabilization energy for the cut through the $1\,^4A_2$ minimum is $E_s[\min(1\,^4A_2)] = 991\,\text{cm}^{-1}$ as indicated in Fig. 8(a) and clarified in Fig. S4 of the Supplemental Material [45]. The localization energy is $E_{\text{loc}} = 225\,\text{cm}^{-1}$.

D. Interactions in the vicinity of the $1\,^4E''$ global minimum

Despite the small transition dipole strengths between the quartet ground state and the first excited quartet state, discussed above [see Fig. 7(b)], we claim that the $1\,^4A_2$ state is a promising candidate for PA experiments. First, its minimum is rather well isolated from intersections with doublet and quartet states (both in C_{2v} and C_s configuration space) due to the low density of states. Only the $2\,^2B_1$ and $3\,^2A_1$ states show intersections, in close proximity to the $1\,^4A_2$ minimum, besides the symmetry-required one with the $1\,^4B_2$ state. The

energetically closest intersection emerges at C_{2v} geometry with the $3\,^2A_1$ state for $R_2 = R_3 \approx 2.65\,\text{Å}$ and $R_1 \approx 1.7\,\text{Å}$. For C_s geometries intersections with the $2\,^2B_1$ state move slightly closer to the minimum of the first excited quartet state while the $3\,^2A_1$ intersections approximately remain at the same location. However, all intersections are $\gtrsim 60\,\text{cm}^{-1}$ away from the $1\,^4A_2$ global minimum. The situation is illustrated in Fig. S5 of the Supplemental Material [45]. As indicated previously, the $1\,^4A_2$ minimum is stabilized from COINs by $E_s[\text{min}(1\,^4A_2)] = 991\,\text{cm}^{-1}$.

In the vicinity of the $1\,^4A_2$ equilibrium geometry SOC effects are rather small vanishing with $1/r$ for large r (with $r \propto \sqrt{Q_2^2 + Q_3^2}$ measuring the distortion from D_{3h} symmetry to acute C_{2v} triangular geometries) as follows from relativistic JT theory [35,79]. Strongest SOCs of the $1\,^4A_2$ state close to its equilibrium geometry are to the quartet ground state $1\,^4B_1$ as well as to the excited state $1\,^4A_1$ with typical magnitudes between 30 and $50\,\text{cm}^{-1}$. The $1\,^4A_1$ state shows a local minimum at $E_{\text{min}}(1\,^4A_1) = 6766\,\text{cm}^{-1}$ (see Table II) and is thus well separated from the $1\,^4A_2$ state. Spin-orbit couplings to doublet states are slightly weaker with interactions between $1\,^4A_2$ and the $2\,^2A_1$, $3\,^2A_1$, $4\,^2A_1$, $5\,^2A_1$, $3\,^2B_1$, and $4\,^2B_1$ states with orders of 10 to $30\,\text{cm}^{-1}$. Those equilibrium states are found either well below the minimum of the $1\,^4A_2$ state at 229 or $1898\,\text{cm}^{-1}$, respectively, or well above, starting from $5431\,\text{cm}^{-1}$ (the corresponding values are taken from Table S.III of the Supplemental Material [45]).

IV. SUMMARY AND OUTLOOK

This paper provides a possible roadmap to the experimental realization of PA processes of single ultracold rubidium trimers. We give a wide-ranging overview of available states using the MRCI method, together with a large-core ECP with CPP and a modified even-tempered valence basis set. By special cuts through the PESs of both low- and high-spin species, we revealed their topology and gave an idea of the mutual position and the expected density of electronic states. We discussed the prominent feature of the (pseudo) JT effect naturally occurring for triangular geometries and outlined Renner-Teller (combined with pseudo Jahn-Teller) interactions for linear geometries. We also provided a survey of SOC effects giving selection rules and showing that they are weak, particularly for the low-lying states involved in possible PA schemes.

We studied the equilibrium states as well as the locations of selected ITPs on the quartet ground-state PES in the configuration space. Since states lying close to ITPs are promising candidates for good Franck-Condon factors this analysis helped us to identify suitable states for PA processes. We focused on the $1\,^4E''$ state (consisting of the lowest-lying excited states $1\,^4A_2$ and $1\,^4B_2$) for which we investigated the characteristic JT topology of the corresponding PES and discussed the consequences of the underlying JT effect. Finally, we investigated the main coupling effects for the first excited quartet state ($1\,^4A_2$), including electronic dipole transition strengths at ITP geometries, intersections to nearby doublet and quartet states, as well as spin-orbit couplings. This confirms the $1\,^4A_2$ state as a promising candidate for PA experiments.

In a next step we will analyze and fix the breakdown of the Born-Oppenheimer approximation, connected to the various Jahn-Teller coupling effects, by means of different diabatization techniques including diabatic PES interpolation approaches.

Data corresponding to the figures are available in the Supplemental Material [45].

[1] G. Quemener and P. Julienne, Chem. Rev. **112**, 4949 (2012).

[2] J. Bohn, A. Rey, and J. Ye, Science **357**, 1002 (2017).

[3] N. Balakrishnan, J. Chem. Phys. **145**, 150901 (2016).

[4] R. V. Krems, Phys. Chem. Chem. Phys. **10**, 4079 (2008).

[5] L. D. Carr, D. DeMille, R. V. Krems, and J. Ye, New J. Phys. **11**, 055049 (2009).

[6] J. Doyle, B. Friedrich, R. V. Krems, and F. Masnou-Seeuws, Eur. Phys. J. D **31**, 149 (2004).

[7] E. A. Burt, R. W. Ghrist, C. J. Myatt, M. J. Holland, E. A. Cornell, and C. E. Wieman, Phys. Rev. Lett. **79**, 337 (1997).

[8] D. M. Stamper-Kurn, M. R. Andrews, A. P. Chikkatur, S. Inouye, H.-J. Miesner, J. Stenger, and W. Ketterle, Phys. Rev. Lett. **80**, 2027 (1998).

[9] C. H. Greene, P. Giannakeas, and J. Pérez-Ríos, Rev. Mod. Phys. **89**, 035006 (2017).

[10] J. Ulmanis, J. Deiglmayr, M. Repp, R. Wester, and M. Weidemüller, Chem. Rev. **112**, 4890 (2012).

[11] K. M. Jones, E. Tiesinga, P. D. Lett, and P. S. Julienne, Rev. Mod. Phys. **78**, 483 (2006).

[12] T. Köhler, K. Góral, and P. S. Julienne, Rev. Mod. Phys. **78**, 1311 (2006).

[13] C. Chin, R. Grimm, P. Julienne, and E. Tiesinga, Rev. Mod. Phys. **82**, 1225 (2010).

[14] O. Dulieu and C. Gabbanini, Rep. Prog. Phys. **72**, 086401 (2009).

[15] R. Kosloff, J. Chem. Phys. **92**, 2087 (1988).

[16] O. Dulieu and P. S. Julienne, J. Chem. Phys. **103**, 60 (1995).

[17] D. T. Colbert and W. H. Miller, J. Chem. Phys. **96**, 1982 (1992).

[18] F. Ferlaino, A. Zenesini, M. Berninger, B. Huang, H.-C. Nägerl, and R. Grimm, Few-Body Syst. **51**, 113 (2011).

[19] G. Delacrétaz, E. R. Grant, R. L. Whetten, L. Wöste, and J. W. Zwanziger, Phys. Rev. Lett. **56**, 2598 (1986).

[20] W. E. Ernst and S. Rakowsky, Ber. Bunsenges. Phys. Chem. **99**, 441 (1995).

[21] D. T. Vituccio, O. Golonzka, and W. E. Ernst, J. Mol. Spectrosc. **184**, 237 (1997).

[22] J. Nagl, G. Auböck, A. W. Hauser, O. Allard, C. Callegari, and W. E. Ernst, J. Chem. Phys. **128**, 154320 (2008).

[23] G. Auböck, J. Nagl, C. Callegari, and W. E. Ernst, J. Chem. Phys. **129**, 114501 (2008).

[24] J. Nagl, G. Auböck, A. W. Hauser, O. Allard, C. Callegari, and W. E. Ernst, Phys. Rev. Lett. **100**, 063001 (2008).

[25] A. W. Hauser and W. E. Ernst, Phys. Chem. Chem. Phys. **13**, 18762 (2011).

[26] C. Giese, F. Stienkemeier, M. Mudrich, A. W. Hauser, and W. E. Ernst, Phys. Chem. Chem. Phys. **13**, 18769 (2011).

[27] R. L. Martin and E. R. Davidson, Mol. Phys. **35**, 1713 (1978).

[28] J. L. Martins, R. Car, and J. Buttet, J. Chem. Phys. **78**, 5646 (1983).

[29] T. C. Thompson, G. J. Izmirlian, S. J. Lemon, D. G. Truhlar, and C. A. Mead, J. Chem. Phys. **82**, 5597 (1985).

[30] F. Cocchini, T. H. Upton, and W. Andreoni, J. Chem. Phys. **88**, 6068 (1988).

[31] F. Spiegelmann and D. Pavolini, J. Chem. Phys. **89**, 4954 (1988).

[32] R. Meiswinkel and H. Köppel, Chem. Phys. **144**, 117 (1990).

[33] R. de Vivie-Riedle, J. Gaus, V. Bonačić-Koutecký, J. Manz, B. Reischl-Lenz, and P. Saalfrank, Chem. Phys. **223**, 1 (1997).

[34] A. W. Hauser, C. Callegari, P. Soldán, and W. E. Ernst, J. Chem. Phys. **129**, 044307 (2008).

[35] A. W. Hauser, G. Auböck, C. Callegari, and W. E. Ernst, J. Chem. Phys. **132**, 164310 (2010).

[36] A. W. Hauser, C. Callegari, P. Soldán, and W. E. Ernst, Chem. Phys. **375**, 73 (2010).

[37] A. W. Hauser, J. V. Pototschnig, and W. E. Ernst, Chem. Phys. **460**, 2 (2015).

[38] A. W. Hauser, C. Callegari, and W. E. Ernst, Level-structure and magnetic properties from one-electron atoms to clusters with delocalized electronic orbitals: Shell models for alkali trimers, in *Advances in the Theory of Atomic and Molecular Systems*, edited by P. Piecuch, J. Maruani, G. Delgado-Barrio, and S. Wilson (Springer, New York, 2009), pp. 201–215.

[39] A. W. Hauser, The electronic structure of alkali trimers in their doublet and quartet manifolds: Shell models and quantum chemistry calculations, Ph.D. thesis, Technische Universität Graz, 2009.

[40] P. Soldán, J. Chem. Phys. **132**, 234308 (2010).

[41] J. Pérez-Ríos, M. Lepers, and O. Dulieu, Phys. Rev. Lett. **115**, 073201 (2015).

[42] J. Wang, J. P. D'Incao, B. D. Esry, and C. H. Greene, Phys. Rev. Lett. **108**, 263001 (2012).

[43] S. Mukherjee and S. Adhikari, Chem. Phys. **440**, 106 (2014).

[44] H. Silberbach, P. Schwerdtfeger, H. Stoll, and H. Preuss, J. Phys. B **19**, 501 (1986).

[45] See Supplemental Material at http://link.aps.org/supplemental/10.1103/PhysRevA.103.022820 for details on technical aspects, which includes Refs. [46–51], or for more detailed tables and figures. Raw data corresponding to all figures shown in this paper can be found there as well.

[46] S. Huzinaga and B. Miguel, Chem. Phys. Lett. **175**, 289 (1990).

[47] S. Huzinaga and M. Klobukowski, Chem. Phys. Lett. **212**, 260 (1993).

[48] D. P. Tew and W. Klopper, J. Chem. Phys. **125**, 094302 (2006).

[49] I. Cherkes, S. Klaiman, and N. Moiseyev, Int. J. Quantum Chem. **109**, 2996 (2009).

[50] P. J. Linstrom and W. G. Mallard, NIST Chemistry WebBook, NIST Standard Reference Database No. 69, 2019, data retrieved https://doi.org/10.18434/T4D303.

[51] D. Bishop, *Group Theory and Chemistry*, Dover Books on Physics and Chemistry (Dover, New York, 1993).

[52] H.-J. Werner and P. J. Knowles, J. Chem. Phys. **89**, 5803 (1988).

[53] P. J. Knowles and H.-J. Werner, Chem. Phys. Lett. **145**, 514 (1988).

[54] P. J. Knowles and H.-J. Werner, Theor. Chim. Acta **84**, 90 (1992).

[55] H.-J. Werner and E. A. Reinsch, J. Chem. Phys. **76**, 3144 (1982).

[56] H.-J. Werner, in *Advances in Chemical Physics*, Vol. 69, edited by K. P. Lawley, (Wiley, New York, 1987), pp. 1–62.

[57] H.-J. Werner, P. J. Knowles, G. Knizia, F. R. Manby, M. Schütz, *et al.*, MOLPRO, version 2018.2, a package of ab initio programs, 2018, http://www.molpro.net.

[58] C. Strauss, T. Takekoshi, F. Lang, K. Winkler, R. Grimm, J. Hecker Denschlag, and E. Tiemann, Phys. Rev. A **82**, 052514 (2010).

[59] H. Salami, T. Bergeman, B. Beser, J. Bai, E. H. Ahmed, S. Kotochigova, A. M. Lyyra, J. Huennekens, C. Lisdat, A. V. Stolyarov, O. Dulieu, P. Crozet, and A. J. Ross, Phys. Rev. A **80**, 022515 (2009).

[60] B. Drews, M. Deiß, J. Wolf, E. Tiemann, and J. Hecker Denschlag, Phys. Rev. A **95**, 062507 (2017).

[61] C. Amiot and J. Verges, Mol. Phys. **61**, 51 (1987).

[62] C. Amiot, J. Chem. Phys. **93**, 8591 (1990).

[63] C. Amiot, Mol. Phys. **58**, 667 (1986).

[64] G.-H. Jeung, J. Mol. Spectrosc. **182**, 113 (1997).

[65] R. Guérout, P. Soldán, M. Aymar, J. Deiglmayr, and O. Dulieu, Int. J. Quantum Chem. **109**, 3387 (2009).

[66] H. Suno, B. D. Esry, C. H. Greene, and J. P. Burke, Phys. Rev. A **65**, 042725 (2002).

[67] A. S. Coolidge and H. M. James, Phys. Rev. **51**, 855 (1937).

[68] C. L. Pekeris, Phys. Rev. **112**, 1649 (1958).

[69] C. L. Pekeris, Phys. Rev. **115**, 1216 (1959).

[70] C. L. Pekeris, B. Schiff, and H. Lifson, Phys. Rev. **126**, 1057 (1962).

[71] C. L. Pekeris, Phys. Rev. **127**, 509 (1962).

[72] Y. Accad, C. L. Pekeris, and B. Schiff, Phys. Rev. A **4**, 516 (1971).

[73] B. Schiff, C. L. Pekeris, and Y. Accad, Phys. Rev. A **4**, 885 (1971).

[74] E. R. Davidson, J. Am. Chem. Soc. **99**, 397 (1977).

[75] I. B. Bersuker, Chem. Rev. **101**, 1067 (2001).

[76] C. M. R. Rocha and A. J. C. Varandas, J. Chem. Phys. **144**, 064309 (2016).

[77] W. Domcke, S. Mishra, and L. V. Poluyanov, Chem. Phys. **322**, 405 (2006).

[78] B. P. Thapaliya, M. B. Dawadi, C. Ziegler, and D. S. Perry, Chem. Phys. **460**, 31 (2015).

[79] T. A. Barckholtz and T. A. Miller, Int. Rev. Phys. Chem. **17**, 435 (1998).

[80] L. V. Poluyanov and W. Domcke, Chem. Phys. **352**, 125 (2008).

[81] Y. Liu, I. B. Bersuker, W. Zou, and J. E. Boggs, Chem. Phys. **376**, 30 (2010).

[82] I. B. Bersuker, Chem. Rev. **113**, 1351 (2013).

[83] J. Wolf, M. Deiß, A. Krükow, E. Tiemann, B. P. Ruzic, Y. Wang, J. P. D'Incao, P. S. Julienne, and J. H. Denschlag, Science **358**, 921 (2017).

[84] I. S. Lim, P. Schwerdtfeger, B. Metz, and H. Stoll, J. Chem. Phys. **122**, 104103 (2005).

[85] M. Dolg, Effective core potentials, in *Modern Methods and Algorithms of Quantum Chemistry*, edited by J. Grotendorst (NIC-Directors, Jülich, 2000), pp. 507–540.

[86] S. Matsika and D. R. Yarkony, J. Chem. Phys. **115**, 2038 (2001).

[87] S. Matsika and D. R. Yarkony, J. Chem. Phys. **115**, 5066 (2001).

[88] S. Matsika and D. R. Yarkony, J. Chem. Phys. **116**, 2825 (2002).